Appl. Phys. B 86, 623–631 (2007)
DOI: 10.1007/s00340-006-2567-5
Applied Physics B
Lasers and Optics

Y.-K. KUO[1,✉]
J.-R. CHEN[2]
M.-L. CHEN[1]
B.-T. LIOU[3]

Numerical study on strained InGaAsP/InGaP quantum wells for 850-nm vertical-cavity surface-emitting lasers

[1] Department of Physics, National Changhua University of Education, Changhua 500, Taiwan
[2] Department of Photonics and Institute of Electro-Optical Engineering, National Chiao-Tung University, Hsinchu 300, Taiwan
[3] Department of Mechanical Engineering, Hsiuping Institute of Technology, Taichung 412, Taiwan

Received: 3 August 2006/Final version: 11 December 2006
Published online: 27 January 2007 • **© Springer-Verlag 2007**

ABSTRACT The physical and optical properties of compressively strained InGaAsP/InGaP quantum wells for 850-nm vertical-cavity surface-emitting lasers are numerically studied. The simulation results show that the maximum optical gain, transparency carrier densities, transparency radiative current densities, and differential gain of InGaAsP quantum wells can be efficiently improved by employing a compressive strain of approximately 1.24% in the InGaAsP quantum wells. The simulation results suggest that the 850-nm InGaAsP/InGaP vertical-cavity surface-emitting lasers have the best laser performance when the number of quantum wells is one, which is mainly attributed to the non-uniform hole distribution in multiple quantum wells due to high valence band offset.

PACS 42.55.Px; 78.20.-e; 78.20.Bh; 78.30.Fs

1 Introduction

Vertical-cavity surface-emitting lasers (VCSELs) have been adopted as ideal light sources for optical interconnects due to several inherent advantages including circular output beam, low beam divergence, high modulation bandwidth, and convenient wafer-level testing [1–3]. Especially, VCSELs operating at 850 nm have become a key component for application in local area networks (LANs) [4–6]. For most 850-nm VCSEL devices, an unstrained GaAs/AlGaAs quantum-well structure is usually utilized. However, it has been proposed that by employing a strained quantum-well structure, semiconductor lasers with a lower threshold current density and higher modulation speed can be achieved because of the reduced in-plane heavy-hole effective mass [7–9]. The InGaAs/AlGaAs, InGaAlAs/AlGaAs, and InGaAsP/InGaP quantum-well structures are usually used in strained 850-nm semiconductor lasers [10]. The strain level of an InGaAs/AlGaAs quantum well emitting near 850 nm is limited due to the use of a narrow quantum well [10]. As for the InGaAlAs/AlGaAs quantum wells, the indium and aluminum compositions can be varied to achieve different strain levels. Nevertheless, employing aluminum in a quantum well may cause the problem of oxidation in active region [11, 12]. Therefore, the use of an aluminum-free InGaAsP/InGaP active region is an attractive alternative for 850-nm VCSELs. Tansu et al. have experimentally demonstrated low-temperature sensitive InGaAsP/InGaP lasers which have a higher characteristic temperature than that of GaAs/AlGaAs lasers [13]. High-speed oxide-confined VCSELs using InGaAsP/InGaP strain-compensated multiple-quantum wells have been demonstrated by other researchers [14, 15]. For the strained InGaAsP/InGaP quantum wells, although the properties of strained $(Al_xGa_{1-x})_yIn_{1-y}As_zP_{1-z}$ material system was theoretically studied for 850-nm surface- and edge-emitting lasers, the amount of compressive strain of the InGaAsP/InGaP quantum well was fixed at 1.7% [10]. To the best of our knowledge, qualitative analysis of varying compressive strain in InGaAsP quantum wells, which have an emission wavelength of ~ 850 nm, has not been well documented in literature.

A gain-cavity detuning of approximately 10 nm is usually introduced for the design of 850-nm VCSELs to result in a flat threshold current versus temperature behavior over some range of temperature operation. In this study, in order to obtain the suitable quantum-well structure for 850-nm VCSELs, compressively strained InGaAsP/InGaP quantum wells emitting at 840 nm with different strains are investigated by an advanced photonic integrated circuit simulator in three dimensions (PICS3D), which self-consistently combines quantum well band structure calculations by $6 \times 6\, k \cdot p$ theory, radiative and nonradiative carrier recombination, carrier drift and diffusion, and optical mode computation [16]. Based on the $6 \times 6\, k \cdot p$ theory, the optical gain spectra, transparency carrier densities, transparency radiative current densities, and maximum differential gain for the InGaAsP quantum wells with different compressive strains are compared and discussed. Furthermore, the optimal number of quantum wells for the strained InGaAsP/InGaP VCSELs is studied as well.

2 Theoretical method and parameters

In this paper, it is assumed that the compressively strained InGaAsP quantum wells are grown on (001)-oriented

✉ Fax: +886-4-721-1153, E-mail: ykuo@cc.ncue.edu.tw

GaAs substrates. For simplicity, it is also supposed that the conduction subbands are decoupled from valence subbands and have isotropic parabolic bands, such as the situation of most III-V direct bandgap semiconductors [17]. The 6×6 Luttinger–Kohn Hamiltonian including the coupling of the heavy hole, light hole, and spin-orbit splitting bands is utilized to evaluate the nonparabolic valence band structures [18]. As for the numerical parameters required for $k \cdot p$ calculations for the InGaAsP materials, except for the unstrained bandgap energies, a linear interpolation between the parameters of the relevant binary semiconductors is utilized. For a physical parameter P, the interpolation formula is [19]

$$P(\mathrm{In}_{1-x}\mathrm{Ga}_x\mathrm{As}_y\mathrm{P}_{1-y}) = P(\mathrm{GaAs})xy + P(\mathrm{GaP})x(1-y) + P(\mathrm{InAs})(1-x)y + P(\mathrm{InP})(1-x)(1-y)\,. \quad (1)$$

The material parameters of the binary semiconductors used in this study are taken from the paper by Vurgaftman et al. [20] and summarized in Table 1. The formula for the calculation of unstrained InGaAsP bandgap energies can be expressed as a weighted sum of the bandgap energies of relevant ternary semiconductors with appropriate bowing parameters. Specifically, the unstrained InGaAsP bandgap energies are calculated by following expressions [20]

$$E_\mathrm{g}(\mathrm{InGaAsP}) = \frac{x(1-x)[(1-y)E_\mathrm{g}(\mathrm{GaInP}) + yE_\mathrm{g}(\mathrm{GaInAs})]}{x(1-x)+y(1-y)} + \frac{y(1-y)[xE_\mathrm{g}(\mathrm{GaAsP}) + (1-x)E_\mathrm{g}(\mathrm{InAsP})]}{x(1-x)+y(1-y)}\,, \quad (2)$$

$$E_\mathrm{g}(\mathrm{GaInP}) = xE_\mathrm{g}(\mathrm{GaP}) + (1-x)E_\mathrm{g}(\mathrm{InP}) - x(1-x)B(\mathrm{GaInP})\,, \quad (3)$$

$$E_\mathrm{g}(\mathrm{GaInAs}) = xE_\mathrm{g}(\mathrm{GaAs}) + (1-x)E_\mathrm{g}(\mathrm{InAs}) - x(1-x)B(\mathrm{GaInAs})\,, \quad (4)$$

$$E_\mathrm{g}(\mathrm{GaAsP}) = yE_\mathrm{g}(\mathrm{GaAs}) + (1-y)E_\mathrm{g}(\mathrm{GaP}) - y(1-y)B(\mathrm{GaAsP})\,, \quad (5)$$

$$E_\mathrm{g}(\mathrm{InAsP}) = yE_\mathrm{g}(\mathrm{InAs}) + (1-y)E_\mathrm{g}(\mathrm{InP}) \; y(1-y)B(\mathrm{InAsP})\,, \quad (6)$$

where x and y represent the compositions of gallium and arsenic in the InGaAsP material system, respectively. The bandgap bowing parameters of GaInP, GaInAs, GaAsP, and InAsP are 0.65 eV, 0.477 eV, 0.19 eV, and 0.1 eV, respectively [20]. Except for GaP, the temperature dependent bandgap energies of the relevant binary semiconductors are calculated using the commonly employed Varshni formula

Parameter (unit)	GaAs	InAs	InP
α (meV/K)	0.5405	0.276	0.363
β (K)	204	93	162
E_g ($T=0$) (eV)	1.519	0.417	1.4236

TABLE 2 Varshni parameters of the binary semiconductors GaAs, InAs, and InP

$$E_\mathrm{g}(T) = E_\mathrm{g}(T=0) - \frac{\alpha T^2}{T+\beta}\,. \quad (7)$$

The values of α, β, and E_g ($T=0$), i.e., the bandgap energy at zero Kelvin, of the binary alloys are listed in Table 2 [20]. The temperature dependent bandgap energy of the GaP is calculated by the expression of $2.886 + 0.1081[1 - \coth(164/T)]$ [20]. The conduction band offset for the compressively strained InGaAsP/InGaP quantum well is set to 18% of the total band offset [21, 22]. The optical gain spectra of single quantum-well structures, with the valence-band-mixing effect being taken into account, can be expressed by [23]

$$g(E) = \frac{2q^2\hbar}{n\varepsilon_0 c m_0^2 L E} \times \sum_{n,m} \int_0^\infty \frac{k_t M_{nm}(k_t)\Gamma/(2\pi)}{\left(E_{cn}(k_t) - E_{kpm}(k_t) - E\right)^2 + (\Gamma/2)^2} \left(f_\mathrm{c}^n - f_\mathrm{v}^m\right) \mathrm{d}k_t\,, \quad (8)$$

where q is the free electron charge, h is the reduced Planck's constant, n is the index of refraction, ε_0 is the free-space dielectric constant, c is the speed of light, L is the thickness of quantum well, E is the photon energy, $M_{nm}(k_t)$ is the momentum matrix element in the strained quantum well, $\Gamma = h/\tau$ is the broadening due to intraband scattering relaxation time τ, E_{cn} is the n-th conduction subband, E_{kpm} is the m-th valence subband from the $k \cdot p$ calculation, f_c^n and f_v^m are the Fermi functions for the conduction band states and the valence band states, respectively. The indices n and m denote the electron states in the conduction band and the heavy hole (light hole) subband states in the valence band. To account for the broadening due to scattering, it is assumed that $\tau = 0.1$ ps [24–27] in the calculations.

The spontaneous emission rate can be expressed as follows [23]

Parameter	Symbol (unit)	GaAs	InAs	GaP	InP
Lattice constant	a_0 (Å)	5.65325	6.0583	5.4505	5.8697
Spin-orbit splitting	Δ_so (eV)	0.341	0.39	0.08	0.108
Luttinger parameter	γ_1	6.98	20.0	4.05	5.08
	γ_2	2.06	8.5	0.49	1.6
	γ_3	2.93	9.2	2.93	2.1
Hydrostatic deformation potential	a (eV)	−8.33	−6.08	−9.9	−6.6
Shear deformation potential	b (eV)	−2.0	−1.8	−1.6	−2.0
Elastic stiffness constant	C_{11} (GPa)	1221	832.9	1405	1011
Elastic stiffness constant	C_{12} (GPa)	566	452.6	620.3	561
Electron effective mass	$m_\mathrm{e}/m_\mathrm{o}$	0.067	0.026	0.13	0.0795

TABLE 1 Material parameters of the binary semiconductors GaAs, InAs, GaP and InP

$$r_{sp}(E) = \frac{2nq^2E}{\pi^2\hbar^2c^3\varepsilon_0 m_0^2 L_z} \times \sum_{n,m} \int_0^\infty \frac{k_t M_{nm}(k_t)\Gamma/(2\pi)}{\left(E_{cn}(k_t) - E_{kpm}(k_t) - E\right)^2 + (\Gamma/2)^2} f_c^n \left(1 - f_v^m\right) \times \mathrm{d}k_t \,. \quad (9)$$

The radiative current density J_{rad} can be calculated from the spontaneous emission spectrum using [23, 26, 27]

$$J_{\mathrm{rad}} = ql \int r_{sp}(E)\,\mathrm{d}E \,, \quad (10)$$

where l is the thickness of the active region. Radiative current density can be used to estimate the injected current density required to achieve laser threshold.

The equations used to describe the carrier transport in VCSEL devices are Poisson's equation,

$$-\nabla\left(\frac{\varepsilon_0\varepsilon}{q}\nabla V\right) = -n + p + N_{\mathrm{D}}(1 - f_{\mathrm{D}}) - N_{\mathrm{A}} f_{\mathrm{A}} \,, \quad (11)$$

and the current continuity equations for electrons and holes,

$$\frac{1}{q}\nabla J_n - R_n + G_n = \frac{\partial n}{\partial t} \,, \quad (12)$$

$$\frac{1}{q}\nabla J_p + R_p - G_p = -\frac{\partial p}{\partial t} \,, \quad (13)$$

where V is the electrostatic potential, ε is the relative permittivity, q is the magnitude of a unit charge, f_{D} and f_{A} are the Fermi functions for donor band states and accepter band states, n and p are the electron and hole concentrations, J_n and J_p are the current densities of electrons and holes, N_{D} and N_{A} are the donor and acceptor concentrations, G_n and R_n are the generation rates and recombination rates for electrons, G_p and R_p are the generation rates and recombination rates for holes, respectively. The calculations of carrier capture and escape from the quantum wells are considered in accordance with the model provided by Romero et al. [28]. For the treatment of device heating, the thermoelectric power and thermal current induced by temperature gradient are solved utilizing the methods provided by Wachutka et al. [29]. Various heat sources, including Joule heat, generation/recombination heat, Thomson heat and Peltier heat, are taken into account in this specific study. More description about the physical models utilized in PICS3D simulation program, which is a useful tool to access new designs or to optimize existing devices after calibrating with specific materials, can be found in [30].

3 Results and discussion

3.1 *Properties of* InGaAsP/InGaP *quantum wells*

To study the effects of compressive strains on the properties of the 840-nm InGaAsP quantum wells, five quantum-well structures including $In_{0.02}Ga_{0.98}As_{0.981}P_{0.019}$, $In_{0.12}Ga_{0.88}As_{0.892}P_{0.108}$, $In_{0.22}Ga_{0.78}As_{0.799}P_{0.201}$, $In_{0.32}Ga_{0.68}As_{0.704}P_{0.296}$, and $In_{0.42}Ga_{0.58}As_{0.607}P_{0.393}$ are systematically studied in this paper, which have corresponding in-plane compressive strains of 0.075%, 0.473%, 0.859%, 1.239%, and 1.615%, respectively. All of the quantum wells have the same thickness of 8 nm and the same barrier layer of $In_{0.49}Ga_{0.51}P$, which is lattice matched to GaAs. Since the indium composition dominates the amount of compressive strain, the indium composition is varied with a fixed step of 10% and the appropriate phosphor composition is chosen in such a way that the emission wavelength of the quantum-well structures resulted from transitions between the lowest conduction subband (C1) and the top valence subband (HH1) is 840 nm.

Figure 1a–e show the valence subband structures for the InGaAsP quantum wells with variant indium and arsenic com-

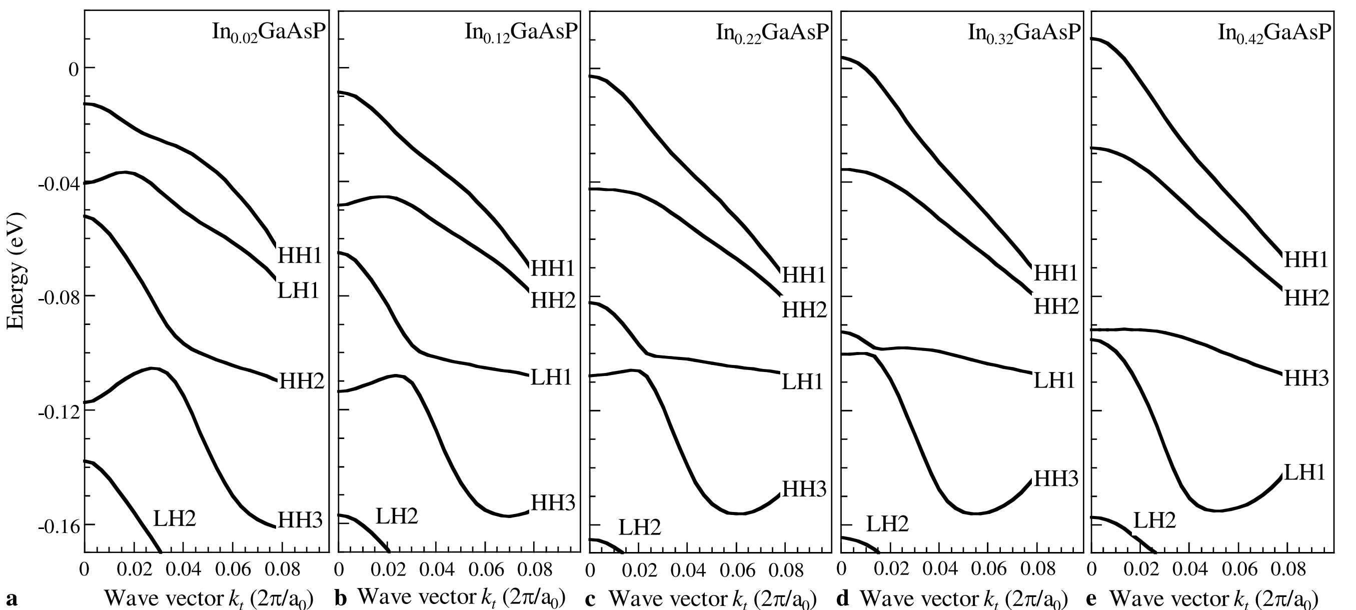

FIGURE 1 Valence subband structures for 8-nm InGaAsP quantum well sandwiched between $In_{0.49}Ga_{0.51}P$ barriers for (**a**) $In_{0.02}Ga_{0.98}As_{0.981}P_{0.019}$, (**b**) $In_{0.12}Ga_{0.88}As_{0.892}P_{0.108}$, (**c**) $In_{0.22}Ga_{0.78}As_{0.799}P_{0.201}$, (**d**) $In_{0.32}Ga_{0.68}As_{0.704}P_{0.296}$, and (**e**) $In_{0.42}Ga_{0.58}As_{0.607}P_{0.393}$

positions as a function of the in-plane wave vector k_t, which is along the horizontal axis and normalized by $2\pi/a_0$. According to these valence-band dispersion curves, the top valence bands are heavy hole subbands in nature due to the compressive strain. In the case of Fig. 1a, the dramatic nonparabolicity observed in the subband structure is a direct result of the band mixing between HH1 and LH1 subbands. When the compressive strain increases with more indium composition in the quantum well, the strain separates the HH1 and LH1 subbands, pushing the LH1 subband away from the HH1. As a result, the band-mixing effects are greatly reduced and the degree of band warping of HH1 is also lower with increasing strain in the quantum wells. Under these circumstances, the effective mass of the holes becomes lighter, which makes the density of states in valence and conduction bands more matched. This condition is expected to result in a much higher differential gain and lower transparency carrier density.

Figure 2a and b show the optical gain spectra of the InGaAsP quantum wells at a fixed carrier density 5×10^{18} cm^{-3} for TE mode at 25 °C and 95 °C. Since the cases of the InGaAsP quantum wells under study are subject to compressive strain, we solely compare the TE mode of different quantum-well structures because the TM mode is strongly depressed with high compressive strain in quantum wells. Besides, the TM mode is mainly introduced by C1-LH1 transition which provides shorter emitting wavelength than 840 nm. Comparing Figs. 1a with 2a, there is a second peak in the gain spectrum of the $In_{0.02}Ga_{0.98}As_{0.981}P_{0.019}$ quantum well due to the smaller separation distance between HH1 and LH1 [see Fig. 1a]. Thus, a portion of the injected carriers will be consumed in the C1-LH1 transitions. On the contrary, the separation distance between HH1 and LH1 increases with compressive strain. This situation leaves more carriers for the C1-HH1 transitions so that the peak gain for TE mode is higher with more compressive strain in the quantum wells. However, it is noteworthy that further increase in material gain becomes minimal when the compressive strain is higher than approximately 1.24%. Furthermore, comparing Fig. 2a with b, the variation of gain peak wavelength with temperature is relatively stable for higher compressively strained quantum well. When the temperature increases from 25 °C to 95 °C, the gain peak wavelength of $In_{0.02}Ga_{0.98}As_{0.981}P_{0.019}$ quantum well (with 0.075% compressive strain) is shifted from 840 nm to 857 nm and that of $In_{0.42}Ga_{0.58}As_{0.607}P_{0.393}$ quantum well (with 1.615% compressive strain) is shifted from 840 nm to 853 nm. The relatively stable variation of gain spectrum with increasing temperature is beneficial for VCSELs operating at high temperature. Figure 2c shows the gain spectra of unstrained GaAs/AlGaAs quantum well at 25 °C and 95 °C. The dashed lines indicate the relevant transition energies (1) C1-LH1 at 25 °C, (2) C1-HH1 at 25 °C, (3) C1-LH1 at 95 °C, and (4) C1-HH1 at 95 °C. Since the valence bands of HH1 and LH1 are close due to the unstrained GaAs/AlGaAs quantum well, the peak gain wavelength becomes shorter than 840 nm at the injection carrier density of 5×10^{18} cm^{-3}, which is attributed to the transition of C1-LH1. When the temperature increases from 25 °C to 95 °C, the peak gain wavelength is shifted by approximately 20 nm, which is larger than that of the InGaAsP/InGaP quantum well.

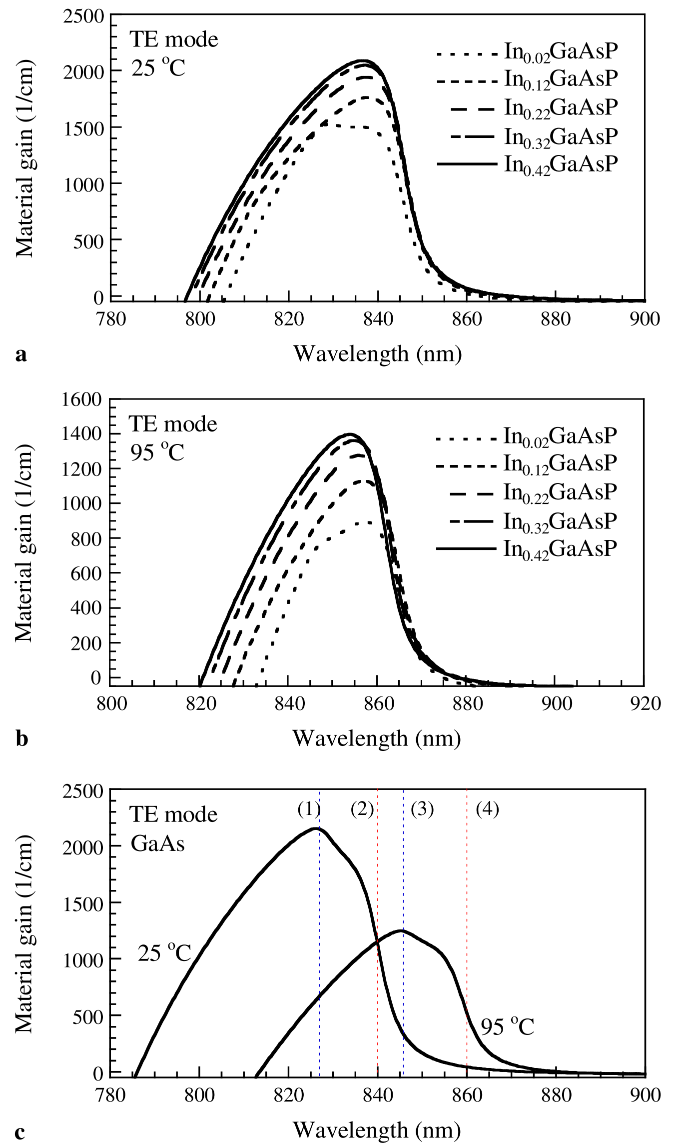

FIGURE 2 Gain spectra of compressively strained InGaAsP/InGaP quantum wells at (**a**) 25 °C and (**b**) 95 °C. (**c**) Gain spectra of unstrained GaAs/AlGaAs quantum well at 25 °C and 95 °C. The *vertical dashed lines* indicate the relevant transition energies (1) C1-LH1 at 25 °C, (2) C1-HH1 at 25 °C, (3) C1-LH1 at 95 °C, and (4) C1-HH1 at 95 °C

Figure 3 depicts the peak material gain of TE mode as a function of carrier density for InGaAsP and unstrained GaAs quantum wells at 25 °C and 95 °C. The thickness of the GaAs quantum well is 8 nm and the barrier is $Al_{0.3}Ga_{0.7}As$. When the compressive strain increases, the transparency carrier density decreases for InGaAsP quantum wells. This is attributed to the higher valence band curvature in the compressively strained quantum well resulting in smaller joint densities of states. Under this situation, the creation of population inversion can be easily achieved [31]. Moreover, the peak material gain increases with the compressive strain in quantum wells. As shown in Fig. 3b, similar trend is observed when the temperature is 95 °C. Compared to unstrained GaAs quantum wells, the strain in InGaAsP quantum wells results in reduced transparency carrier density due to the smaller density of valence states. This also gives

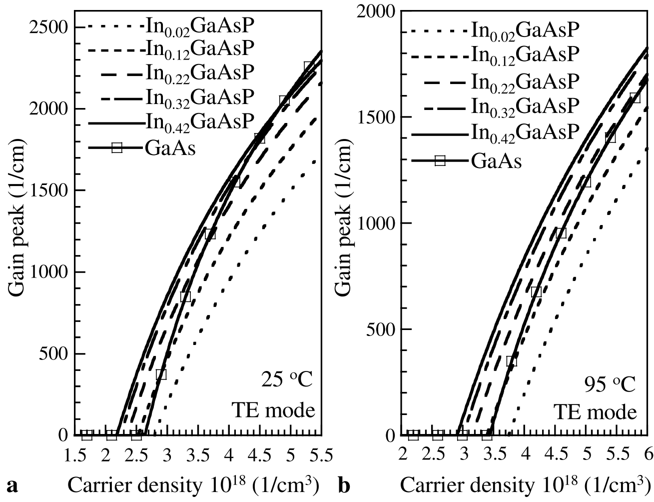

FIGURE 3 Peak material gain of TE mode as a function of carrier density for InGaAsP/InGaP and GaAs/AlGaAs quantum wells at (**a**) 25 °C and (**b**) 95 °C

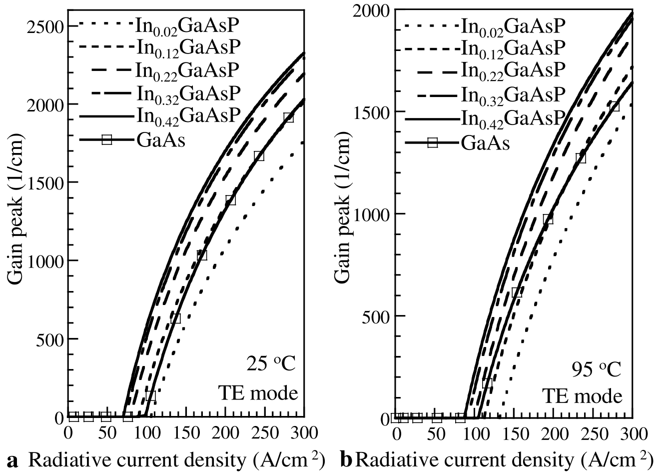

FIGURE 4 Peak material gain of TE mode as a function of radiative current density for InGaAsP/InGaP and GaAs/AlGaAs quantum wells at (**a**) 25 °C and (**b**) 95 °C

rise to gain compression at higher carrier density since the carriers which occupy high energy states do not contribute to the gain maximum. In addition, the transparency carrier density of the GaAs quantum well is lower than that of the $In_{0.02}Ga_{0.98}As_{0.981}P_{0.019}$ quantum well (with 0.075% compressive strain). It is mainly attributed to the minimal strain-induced improvement under this small strain level. Figure 4 shows the peak material gain of TE mode as a function of radiative current density for InGaAsP and GaAs quantum wells at 25 °C and 95 °C. The transparency radiative current density decreases when the composition of indium in quantum wells increases for InGaAsP quantum wells. It can be concluded according to Figs. 3 and 4 that higher compressive strain in quantum wells results in lower transparency carrier density and transparency radiative current density and higher peak material gain. Nevertheless, it is noteworthy that the peak material gain in the range of carrier density and radiative current density under study does not have evident change when the amount of the compressive strain is higher than approximately 1.24%.

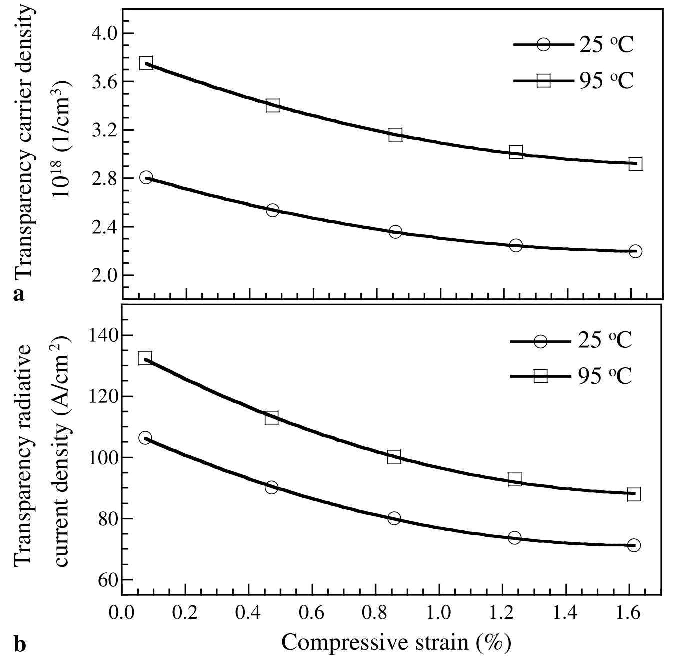

FIGURE 5 (**a**) Transparency carrier density and (**b**) transparency radiative current density of TE mode as a function of compressive strain at 25 °C and 95 °C

For convenient comparison among the properties of InGaAsP quantum wells with different compressive strains, the transparency carrier densities and transparency radiative current densities at 25 °C and 95 °C are depicted as a function of the compressive strain in InGaAsP quantum wells in Fig. 5. The decrease of transparency carrier density and transparency radiative current density with an increase in compressive strain at 25 °C and 95 °C becomes less apparent when the compressive strain in quantum wells is larger than about 1.24%. This can be explained with the valence subband structures of InGaAsP quantum wells, as shown in Fig. 1. The band curvature of the HH1 subband, which dominates the transition in the case of compressively strained quantum wells, does not change evidently when the compressive strain is larger than $\sim 1.24\%$. It means that the density of states near the top of valence band does not change obviously when the compressive strain in quantum wells is higher than $\sim 1.24\%$. Moreover, since the transparency carrier density is primarily decided by the Bernard–Duraffourg inversion condition [7]

$$(F_c - F_v) > \hbar\omega \geq E_g\,, \qquad (14)$$

which requires that the separation between quasi-Fermi levels be greater than the bandgap, the value of $(F_c - F_v)$ is sensitive to the density of states near the top of the valence band when the carriers are injected into the quantum wells. Therefore, the characteristics of the InGaAsP quantum wells under study do not vary markedly when the compressive strain in quantum wells is higher than approximately 1.24%.

The differential gain is one of the most important parameters for high-speed optical interconnects because the relaxation resonance frequency of the laser depends primarily on the square root of the differential gain [19]. Therefore, the calculated values of the maximum differential gain are plotted

as a function of the compressive strain in quantum wells at 25 °C and 95 °C in Fig. 6 and the corresponding carrier densities at which the maximum differential gains are achieved are tabulated in Table 3. Evidently, the maximum differential gain increases with the compressive strain in quantum wells. As expected, the increase of maximum differential gain with more compressive strain in quantum wells becomes less evident when the compressive strain is higher than approximately 1.24% as well. Thus, the variation of valence subband structures with the amount of compressive strain in quantum wells still plays an important role for the differential gain of InGaAsP quantum wells.

It should be mentioned here that, although the optical properties of compressively strained InGaAsP quantum wells can be improved by introducing larger amount of compressive strain in quantum wells, the amount of strain in quantum wells will be limited by the critical thickness for practical crystal growth. Therefore, in order to estimate the critical thicknesses of the five quantum-well structures under study, the Matthews and Blakeslee model [32], which has been used to evaluate the critical thickness of many material systems [33–36], is utilized. In the calculations, the lattice constants and elastic constants are taken from Table 1. The calculated values of the critical thicknesses for the five quantum-well structures under study are tabulated in Table 4. It is evident that the thickness of quantum wells used in this study is well below the critical thicknesses of the five quantum-well structures. Therefore, according to the simulation results, a compressive strain of approximately 1.24% in quantum wells is beneficial for the InGaAsP/InGaP quantum wells for 850-nm vertical-cavity surface-emitting lasers.

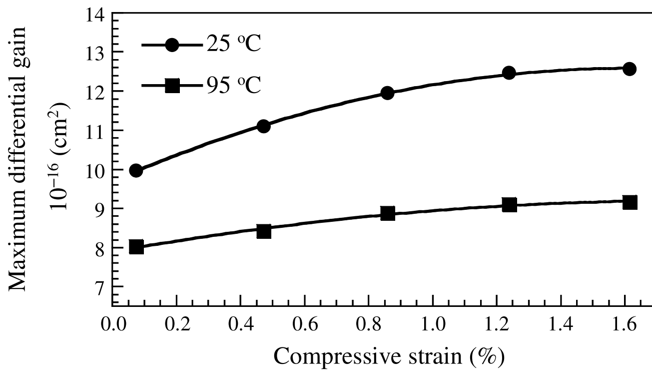

FIGURE 6 Maximum differential gain of TE mode as a function of compressive strain at 25 °C and 95 °C

Quantum well structures	Carrier density (25 °C)	Carrier density (95 °C)
$In_{0.02}Ga_{0.98}As_{0.981}P_{0.019}$	2.76×10^{18} (1/cm^3)	3.72×10^{18} (1/cm^3)
$In_{0.12}Ga_{0.88}As_{0.892}P_{0.108}$	2.50×10^{18} (1/cm^3)	3.36×10^{18} (1/cm^3)
$In_{0.22}Ga_{0.78}As_{0.799}P_{0.201}$	2.32×10^{18} (1/cm^3)	3.12×10^{18} (1/cm^3)
$In_{0.32}Ga_{0.68}As_{0.704}P_{0.296}$	2.21×10^{18} (1/cm^3)	2.98×10^{18} (1/cm^3)
$In_{0.42}Ga_{0.58}As_{0.607}P_{0.393}$	2.16×10^{18} (1/cm^3)	2.88×10^{18} (1/cm^3)

TABLE 3 Carrier densities required to achieve the maximum differential gains at 25 °C and 95 °C

Quantum well structures	Compressive strain	Critical thickness
$In_{0.02}Ga_{0.98}As_{0.981}P_{0.019}$	0.075%	478.7 nm
$In_{0.12}Ga_{0.88}As_{0.892}P_{0.108}$	0.473%	55.9 nm
$In_{0.22}Ga_{0.78}As_{0.799}P_{0.201}$	0.859%	27.1 nm
$In_{0.32}Ga_{0.68}As_{0.704}P_{0.296}$	1.239%	17.1 nm
$In_{0.42}Ga_{0.58}As_{0.607}P_{0.393}$	1.615%	12.2 nm

TABLE 4 Calculated critical thicknesses of InGaAsP quantum wells with Matthews and Blakeslee model

3.2 *Device properties and optimal number of quantum wells*

After investigating the properties of InGaAsP/InGaP quantum-well structures, we calculate and discuss the performance of the VCSELs with the InGaAsP quantum wells under study in an attempt to analyze the detailed optical properties and obtain the optimal number of quantum wells. The p-type and n-type distributed Bragg reflectors (DBRs) consist of $Al_{0.15}Ga_{0.85}As/Al_{0.9}Ga_{0.1}As$ pairs, which have a thickness of a quarter of a wavelength for each layer. The p-type DBR and n-type DBR are typically constructed using 23 and 35 pairs, respectively. The active region consists of 8-nm InGaAsP quantum wells embedded in 10-nm InGaP barriers. The $Al_{0.6}Ga_{0.4}As$ spacer layers are employed so that the cavity

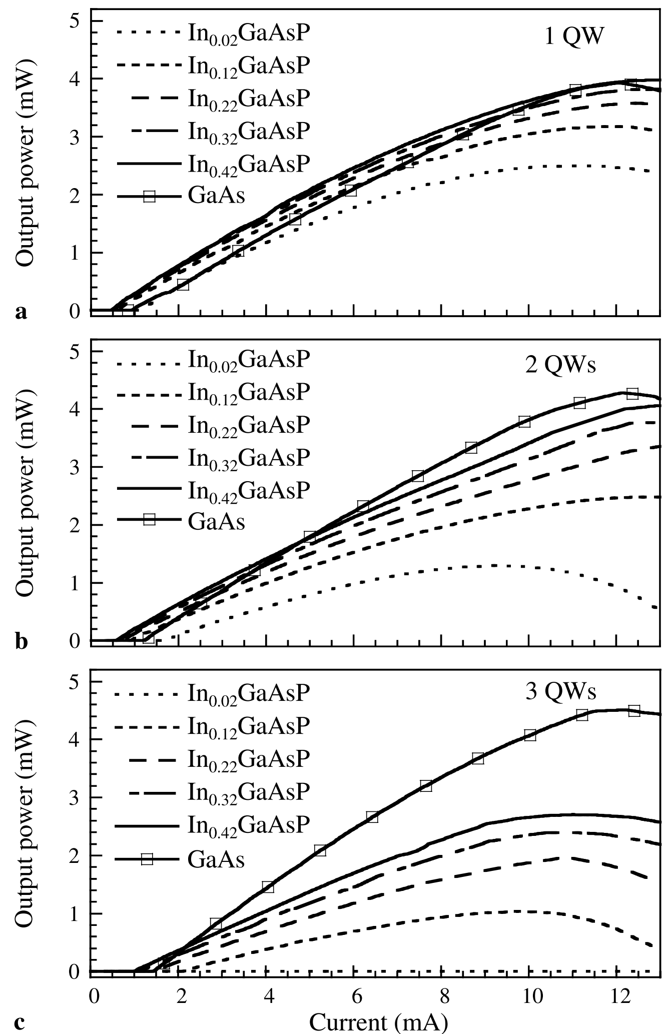

FIGURE 7 Laser output power of the InGaAsP/InGaP and GaAs/AlGaAs VCSELs as a function of current: (**a**) one quantum well, (**b**) two quantum wells, (**c**) three quantum wells

is one wavelength in length. The oxide aperture has a diameter of 5 μm.

Figure 7 shows the laser output power of the InGaAsP/InGaP VCSELs as a function of current when the number of quantum wells varies from one to three. For comparison, the results of the GaAs/AlGaAs VCSEL are also plotted in this figure. The simulation results indicate that the best laser performance is obtained when the number of quantum wells is one and the worst laser performance is observed when the number of quantum wells is three for InGaAsP/InGaP quantum wells. Moreover, the threshold current and maximum output power can be improved with increased compressive strain in the InGaAsP quantum wells. The decrease of threshold current and the increase of maximum output power are not obvious when the amount of compressive strain is beyond 1.24%, which is consistent with previous simulation results shown in Sect. 3.1. In the case of GaAs/AlGaAs VCSEL, the maximum output power can be obtained when the number of quantum wells is three. The output power and threshold current are simultaneously increased with the number of quantum wells. The threshold currents of the VCSELs with $In_{0.32}Ga_{0.68}As_{0.704}P_{0.296}$ and $In_{0.42}Ga_{0.58}As_{0.607}P_{0.393}$ quantum wells are always lower than those of the VCSEL with GaAs quantum wells. Furthermore, it is found that the input current at which the maximum output power for GaAs/AlGaAs VCSELs is achieved is approximately 12 mA. As for the InGaAsP/InGaP VCSELs, the input current at which the maximum output power is achieved varies and depends mainly on the number of quantum wells and the amount of strain. However, the output power roll-off is in similar current range for GaAs and InGaAsP VCSELs. Note that the output power roll-off is typically attributed to the self-heating in continuous-wave operation. For VCSELs, the Joule heat in highly resistive p-doped regions dominates the power budget, which is the major factor for device heating [30]. In this study, since the VCSEL structures are the same except for the quantum-well region (GaAs or InGaAsP), the self-heating behavior is expected to be similar in simulation. The use of different quantum-well structures impacts mainly on the threshold current and slope efficiency of the VCSELs.

In order to understand the mechanism which results in the worst laser performance in the case of three quantum wells, the energy band diagrams and electron and hole concentration distributions of the $In_{0.32}Ga_{0.68}As_{0.704}P_{0.296}$/InGaP and GaAs/AlGaAs VCSELs are depicted in Fig. 8 when the number of quantum wells varies from one to three. It is found that the hole concentration distribution is extremely non-uniform in the active region of triple quantum-well VCSEL due to the relatively high valence band offset. The holes are mainly confined in the well closest to the p-side. Therefore, the electrons are attracted by Coulomb force and also confined in this

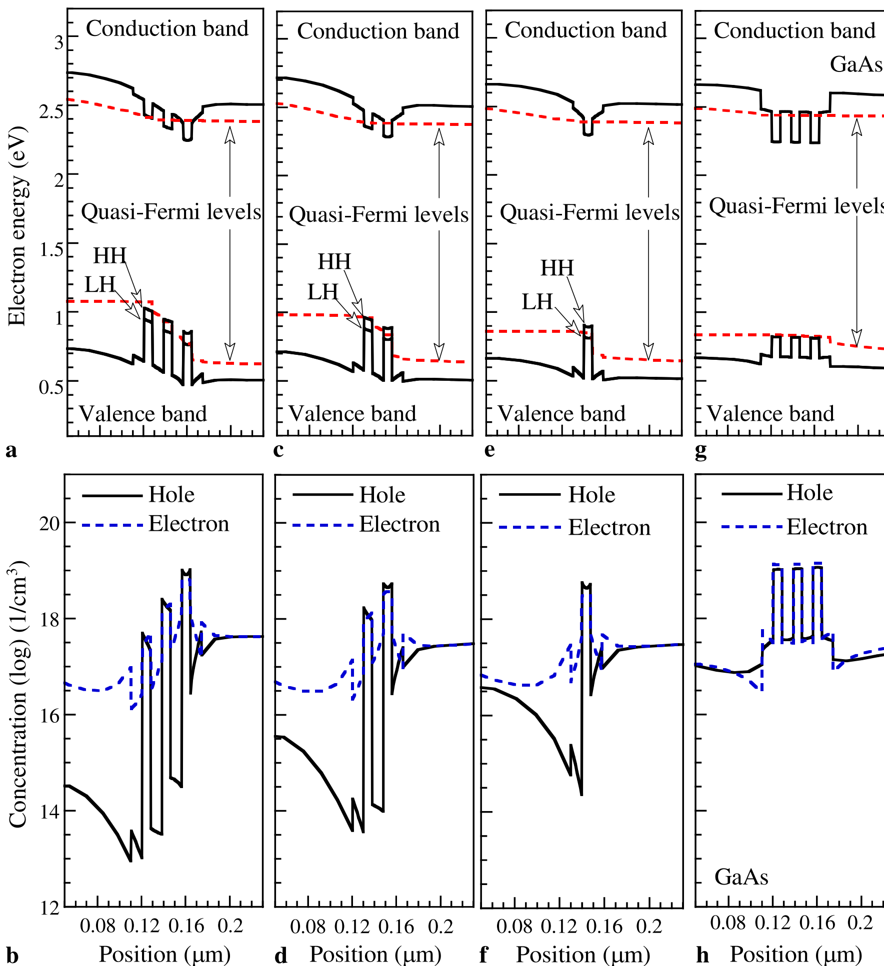

FIGURE 8 Energy band diagrams of the $In_{0.32}Ga_{0.68}As_{0.704}P_{0.296}$/InGaP VCSEL with (**a**) three quantum wells, (**c**) two quantum wells, and (**e**) one quantum well. Electron and hole concentration distributions of the $In_{0.32}Ga_{0.68}As_{0.704}P_{0.296}$/InGaP VCSEL with (**b**) three quantum wells, (**d**) two quantum wells, and (**f**) one quantum well. The energy band diagrams and electron and hole concentration distributions of triple GaAs/AlGaAs quantum-well VCSEL are shown as well. The input current is 13 mA

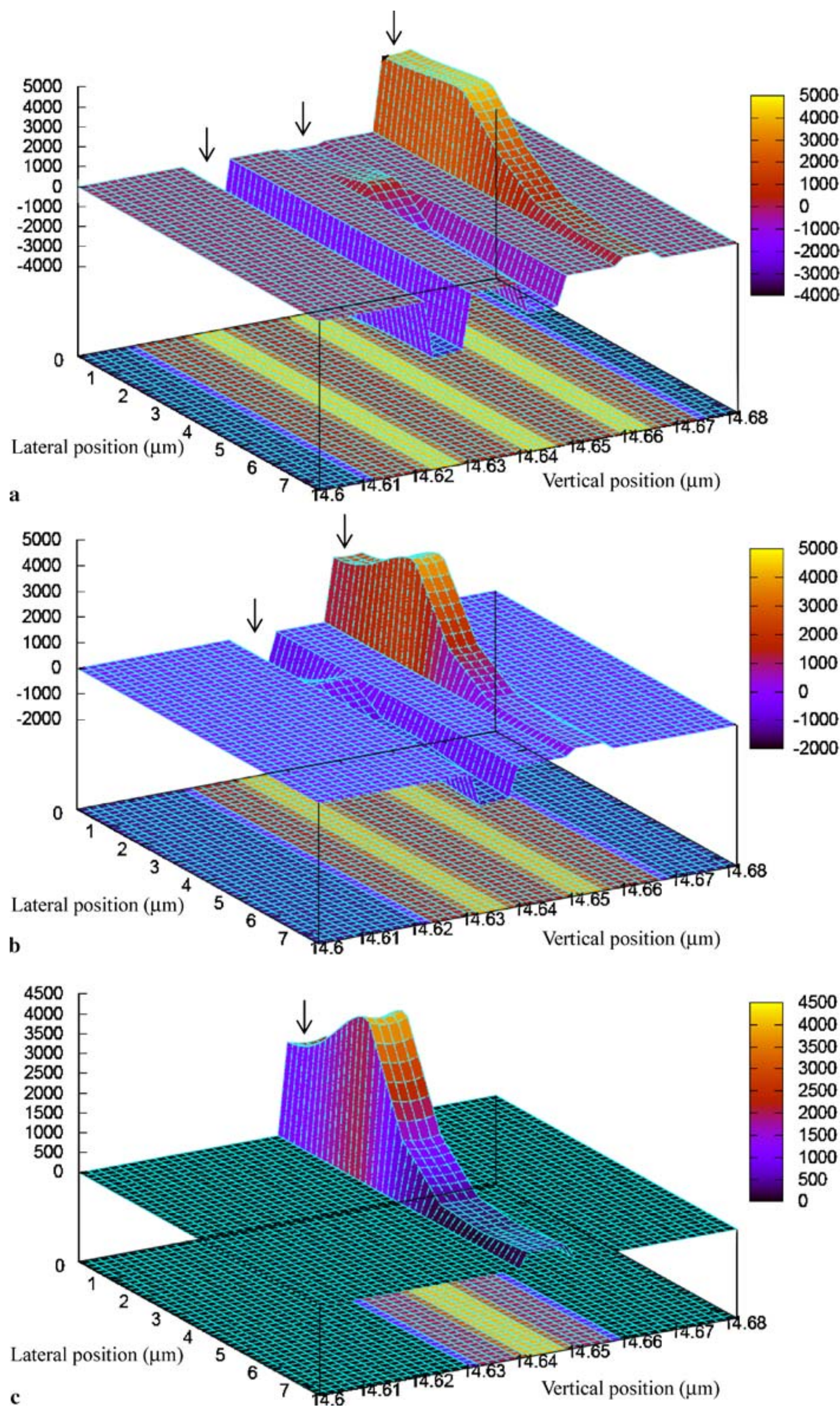

FIGURE 9 Two-dimensional surface plot of the interband gain (1/cm) in the active region of the $In_{0.32}Ga_{0.68}As_{0.704}P_{0.296}$/InGaP VCSEL at an input current of 13 mA: (**a**) three quantum wells, (**b**) two quantum wells, (**c**) one quantum well. The *block arrows* show the positions of the quantum wells

quantum well. Under these circumstances, electrons and holes recombine mostly in the quantum well closest to the p-side. The other two quantum wells can not effectively contribute to light emission because of the low electron and hole concentrations. On the contrary, negative interband gain is observed in these two quantum wells as shown in Fig. 9a. Since the VCSEL structures under study are designed to have an aperture diameter of 5 μm, the interband gain decreases with lateral position due to the oxide-confined layer, as shown in Fig. 9. Furthermore, spatial hole burning can be found more obviously in the single quantum-well VCSEL than in the double and triple quantum-well VCSELs, which indicates that the resonant optical power in the center of the lateral position and stimulated recombination rate are higher in single quantum-well VCSEL. In the case of double quantum-well VCSELs, although the laser performance has been enhanced as com-

pared with the triple quantum-well VCSELs, the negative interband gain is observed in Fig. 9b. Therefore, the simulation results indicate that the 850-nm InGaAsP/InGaP VCSELs have the best laser performance when the number of quantum wells is one because the high valence band offset results in the non-uniform hole concentration distribution in multiple quantum-well structures. As for the triple GaAs/AlGaAs quantum-well VCSEL, the uniform electron and hole concentration distribution enhances the output power obviously as compared with the triple InGaAsP/InGaP quantum-well VCSELs (see Fig. 7c, Fig. 8g and h). However, it is worth noting that the compressively strained InGaAsP/InGaP quantum well is still superior to the unstrained GaAs/AlGaAs quantum well for obtaining a VCSEL of low threshold current.

4 Conclusion

We have investigated the properties of the compressively strained InGaAsP quantum well structures emitting at 840 nm by solving the $6 \times 6\, k \cdot p$ Hamiltonian. The simulation results indicate that, among the active layer structures under study, relatively high optical gain and differential gain, and low transparency carrier density and transparency radiative current density can be achieved by increasing the amount of compressive strain in quantum wells. However, further improvement of the optical gain and threshold properties of the quantum-well structures becomes minimal when the compressive strain in quantum wells is higher than 1.24%. On the other hand, the simulation results also suggest that the laser performance of the InGaAsP/InGaP VCSELs can be efficiently improved when the InGaAsP quantum wells have a compressive strain of 1.24%. Furthermore, the simulation results show that the strained InGaAsP/InGaP VCSELs have the best laser performance when the number of quantum wells is one. Therefore, a compressive strain of 1.24% in the quantum well of a single quantum-well InGaAsP/InGaP VCSEL is suitable for application in 850-nm vertical-cavity surface-emitting lasers.

ACKNOWLEDGEMENTS This work is supported by the National Science Council of Taiwan under grants NSC-94-2112-M-018-009 and NSC-94-2112-M-164-004.

REFERENCES

1 K. Iga, IEEE J. Sel. Top. Quantum Electron. **QE-6**, 1201 (2000)
2 W.W. Chow, K.D. Choquette, M.H. Crawford, K.L. Lear, G.R. Hadley, IEEE J. Quantum Electron. **33**, 1810 (1997)
3 E. Towe, R.F. Leheny, A. Yang, IEEE J. Sel. Top. Quantum Electron. **QE-6**, 1458 (2000)
4 J.S. Gustavsson, A. Haglund, J. Bengtsson, A. Larsson, IEEE J. Quantum Electron. **38**, 1089 (2002)
5 D. Wiedenmann, R. King, C. Jung, R. Jäger, R. Michalzik, P. Schnitzer, M. Kicherer, K.J. Ebeling, IEEE J. Sel. Top. Quantum Electron. **5**, 503 (1999)
6 F.H. Peters, M.H. MacDougal, IEEE Photon. Technol. Lett. **13**, 645 (2001)
7 E. Yablonovitch, E.O. Kane, IEEE J. Lightwave Technol. **6**, 1292 (1988)
8 E.P. O'Reilly, A.R. Adams, IEEE J. Quantum Electron. **QE-30**, 366 (1994)
9 T.R. Chen, B. Zhao, L. Eng, Y.H. Zhoung, J. O'Brien, A. Yariv, Electron. Lett. **29**, 1525 (1993)
10 T.E. Sale, C. Amamo, Y. Ohiso, T. Kurokawa, Appl. Phys. Lett. **71**, 1002 (1997)
11 J.S. Roberts, J.P.R. David, L. Smith, P.L. Tihanyi, J. Cryst. Growth **195**, 668 (1998)
12 L.J. Mawst, S. Rusli, A. Al-Muhanna, J.K. Wade, IEEE J. Sel. Top. Quantum Electron. **5**, 785 (1999)
13 N. Tansu, D. Zhou, L.J. Mawst, IEEE Photon. Technol. Lett. **12**, 603 (2000)
14 H.C. Kuo, Y.S. Chang, F.I. Lai, T.H. Hsueh, Electron. Lett. **39**, 1051 (2003)
15 Y.H. Chang, H.C. Kuo, F.I. Lai, Y.A. Chang, C.Y. Lu, L.H. Laih, S.C. Wang, IEEE J. Lightwave Technol. **22**, 2828 (2004)
16 PICS3D by Crosslight Software, Inc., Burnaby, Canada, 2005 (http://www.crosslight.com)
17 C.-S. Chang, S.L. Chuang, IEEE J. Sel. Top. Quantum Electron. **1**, 218 (1995)
18 Y.-P. Chao, S.L. Chuang, Phys. Rev. B **46**, 4110 (1992)
19 J. Minch, S.H. Park, T. Keating, S.L. Chuang, IEEE J. Quantum Electron. **QE-35**, 771 (1999)
20 I. Vurgaftman, J.R. Meyer, L.R. Ram-Mohan, J. Appl. Phys. **89**, 5815 (2001)
21 Y.-H. Cho, K.-S. Kim, S.-W. Ryu, S.-K. Kim, B.-D. Choe, H. Lim, Appl. Phys. Lett. **66**, 1785 (1995)
22 Y.-H. Cho, B.-D. Choe, H. Lim, Appl. Phys. Lett. **69**, 3740 (1996)
23 S.L. Chuang, *Physics of Optoelectronic Devices* (Wiley, New York, 1995)
24 D. Ahn, S.L. Chuang, Y.-C. Chang, J. Appl. Phys. **64**, 4056 (1988)
25 D. Ahn, S.L. Chuang, IEEE J. Quantum Electron. **QE-26**, 13 (1990)
26 J.C.L. Yong, J.M. Rorison, I.H. White, IEEE J. Quantum Electron. **QE-38**, 1553 (2002)
27 W.J. Fan, S.T. Ng, S.F. Yoon, M.F. Li, T.C. Chong, J. Appl. Phys. **93**, 5836 (2003)
28 B. Romero, J. Arias, I. Esquivias, M. Cada, Appl. Phys. Lett. **76**, 1504 (2000)
29 G.K. Wachutka, IEEE Trans. Comput.-Aided Des. Integr. Circuits Syst. **9**, 1141 (1990)
30 J. Piprek, *Semiconductor Optoelectronic Device: Introduction to Physics and Simulation* (Academic Press, San Diego, 2003)
31 W.W. Chow, E.D. Jones, N.A. Modine, A.A. Allerman, S.R. Kurtz, Appl. Phys. Lett. **75**, 2891 (1999)
32 J.W. Matthews, A.E. Blakeslee, J. Cryst. Growth **27**, 118 (1974)
33 X. Wu, J.-M. Baribeau, J.A. Gupta, M. Beaulieu, J. Cryst. Growth **282**, 18 (2005)
34 Y.-C. Liang, H.-Y. Lee, H.-J. Liu, C.-K. Huang, T.-B. Wu, J. Cryst. Growth **279**, 114 (2005)
35 T. Kitatani, A. Taike, M. Aoki, J. Cryst. Growth **273**, 19 (2004)
36 H.C. Kuo, H.H. Yao, Y.H. Chang, Y.A. Chang, M.Y. Tsai, J. Hsieh, E.Y. Chang, S.C. Wang, J. Cryst. Growth **272**, 538 (2004)